

A correlation-based continuous window-shift technique to reduce the peak-locking effect in digital PIV image evaluation

L. Gui, S. T. Wereley

506

Abstract In this paper the peak-locking phenomenon is investigated in the evaluation of digital PIV recordings by using a correlation-based interrogation algorithm with a discrete window shift and a correlation-based tracking algorithm. Statistical analyses indicate that nonuniformly distributed bias errors are the main cause of the peak-locking effect, and the amplitude variation of the random error is also an important source of the peak locking. Simulations and experimental examples demonstrate that very strong peak-locking effects exist for the correlation-based interrogation algorithm with discrete window shift in the cases of large particle images, small interrogation windows, and very small particle images. Very strong peak-locking effects are also observed for the correlation-based tracking algorithm when the particle images are overexposed, binarized, or very small. These strong peak-locking effects can be avoided without loss of evaluation accuracy by using a continuous window-shift technique in combination with the correlation-based interrogation algorithm.

Abbreviations

FFT	fast Fourier transformation
RMS	root-mean-square
DDF	distribution density function
FCTR	FFT-accelerated correlation-based tracking algorithm
CDWS	correlation-based interrogation algorithm with discrete window shift
CCWS	correlation-based interrogation algorithm with continuous window shift

1

Introduction

The correlation-based interrogation algorithm has been widely used to evaluate PIV recordings since the first application of the digital PIV technique. Correlation-based interrogation schemes and details of the respective pro-

cedures were described, discussed, and reviewed by Cenedese and Paglialunga (1990), Keane and Adrian (1990), Adrian (1991), Willert and Gharib (1991), Heckmann et al. (1994), and Westerweel et al. (1996). For a single exposed PIV recording pair, the correlation-based interrogation algorithm is applied to two small image fractions (samples) of the same size. Traditionally, the two evaluation samples are chosen, respectively, from the first and second images in the PIV recording pair at the same position in the recording coordinate. The evaluation function is simply written as

$$\Phi_{\text{cor}}(m, n) = \sum_{i=1}^M \sum_{j=1}^N g_1(i, j) \cdot g_2(i + m, j + n) , \quad (1)$$

where $g_1(i, j)$ and $g_2(i, j)$ are gray-value distributions of the two evaluation samples, which are restricted in a rectangular interrogation window of size of $M \times N$ pixels. When the computation of the correlation coefficient $\Phi_{\text{cor}}(m, n)$ is accelerated with the fast Fourier transformation (FFT), $g_1(i, j)$ and $g_2(i, j)$ are assumed to be distributed periodically in the i - j -plane with the periodicity M, N . The assumption of periodicity enables a fast evaluation of the PIV recordings, and it makes the correlation-based interrogation algorithm insensitive to the illumination difference between the two PIV recordings in a pair (Gui and Merzkirch 2000). However, the use of the FFT also has disadvantages, such as large evaluation errors at large particle image displacements and large bias gradient around the zero displacement, which increase the measurement uncertainties of the mean velocities and Reynolds stresses, respectively, in turbulent flow measurements (Gui et al. 2001). In order to avoid the large evaluation error at large particle image displacement, a discrete window shift is applied (Willert 1996; Westerweel et al. 1997). To reduce the bias error and the bias gradient around the zero displacement, a Gaussian window mask is adopted (Gui et al. 2000).

The correlation function in (1) has also been used as a tracking criterion to determine the displacement of an image pattern that contains a group of particle images. The correlation-based tracking schemes were described and applied by Huang et al. (1993), Kemmerich and Rath (1994), Okamoto et al. (1995), and Fincham and Spedding (1997). When using the correlation-based tracking algorithm, the gray-value distribution $g_2(i, j)$ is defined in an area larger than the $M \times N$ -pixel interrogation window. Since the periodicity assumption is no longer necessary, greater accuracy can be achieved at large particle image

Received: 2 July 2001 / Accepted: 28 November 2001

L. Gui (✉), S. T. Wereley
Mechanical Engineering, Purdue University
West Lafayette, IN 47907-1288, USA
e-mail: lcgui@yahoo.com

This work was supported by the Indiana 21st Century Research and Technology Fund. Thanks to Prof. R.J. Adrian, Dr. F. Richard and Mr. K. Christian for providing PIV image samples and valuable suggestions.

displacement, and the large bias error and bias gradient around zero displacement can be avoided. To further increase the accuracy and reliability of the correlation-based tracking algorithm, the mean gray values are subtracted from the evaluation samples in the evaluation function as

$$\Phi_{\text{ctr}}(m, n) = \sum_{i=1}^M \sum_{j=1}^N [g_1(i, j) - \bar{g}_1] \cdot [g_2(i + m, j + n) - \bar{g}_2]. \quad (2)$$

The computation of the correlation coefficient $\Phi_{\text{ctr}}(m, n)$ can also be accelerated with FFT by using a zero-padding technique. Wereley and Meinhart (2001) suggested a central-difference discrete window-shift technique for the correlation-based tracking algorithm to avoid additional bias errors in high spatial gradient flow measurements.

Currently, the correlation-based interrogation algorithm with discrete window shift (CDWS) and the FFT-accelerated correlation-based tracking algorithm (FCTR) are the most widely used evaluation algorithms for both standard and micro-PIV. Since the correlation functions Φ_{cor} and Φ_{ctr} are discrete distributions, the subpixel displacement is usually computed with a three-point Gaussian fit. This approximation makes the evaluation error distributions on the particle image displacement into almost periodic functions with a period of one pixel for both CDWS and FCTR. Usually, the minimum errors are located at integer-pixel positions, and the maximum errors are at the midpixel positions. The most commonly observed phenomenon resulting from the nonuniformly distributed evaluation errors is the peak-locking effect, i.e. the magnitudes of the evaluated particle image displacements concentrate at integer values. The peak-locking effect reflects PIV measurement uncertainty and may even cause misinterpretation in the study of turbulent structures. Many researchers have tried to reduce the peak-locking effect by adjusting data in the postprocessing procedure, e.g. Roth and Katz (2001). New methods are also expected to avoid the large evaluation errors that may occur in addition to the peak-locking problem. As discussed by Fei et al. (1999) and Gui and Merzkirch (2000), the FCTR algorithm has large evaluation errors in the cases of low particle image density and large particle image diameter. The CDWS algorithm has very small evaluation error around integer pixels, but very large error at midpixel positions (Westerweel et al. 1997, Westerweel 2000). The Gaussian window mask technique can effectively reduce the bias error of CDWS, but it produces larger random error or requires a larger interrogation window (Gui et al. 2001). In the present work, the authors try to explain the mechanism of the peak-locking phenomenon and use a continuous window-shifting technique not only to minimize the peak-locking effect directly in the basic evaluation step, but also to further reduce the evaluation errors.

The concept of continuous window shifting in PIV evaluation is not a totally new idea. Sjö Dahl (1994) and Sholl and Soras (1997) have implemented the idea of continuous window shifting. When an iterated evaluation scheme is used to consider particle image distortion, a continuous window-shifting feature is automatically

implemented (Huang et al. 1993; Wereley et al. 2001; Wereley and Gui 2001). The effect of continuous window shifting on the peak-locking phenomenon was quantitatively evaluated by Lecordier et al. (1999, 2001). In the present work, the continuous window-shifting technique is combined with the correlation-based interrogation algorithms to make use of the high accuracy of the PIV algorithm near zero displacement.

Most of the discussions in this paper are based on statistical analyses of evaluation results of synthetic PIV recordings using competing algorithms. The synthetic particle images have a Gaussian gray-value profile and are randomly distributed in the simulated PIV recordings of size of 1024×1024 pixels. In the following, the brightness of a particle image is defined as the gray value in its center; the particle image diameter is determined at the mid-brightness cross section (FWHM); and the particle image number density is defined as the number of particles in a 32×32 -pixel window. Two kinds of particle image displacements are simulated in the synthetic PIV recording pairs, i.e. the whole pattern of the synthetic images is displaced in a parallel fashion to determine the dependences of the errors on the particle image displacement, or it is rotated by $\pi/360$ around the image center to simulate a uniform distribution density of the particle image displacements in the region of $[-4, 4]$ pixels. The background of the synthetic PIV recording is assumed to have random noise, i.e. the brightness of every single pixel varies independently and randomly from 0 to a certain gray value, which is called the intensity of the background noise in the following text.

2

Correlation-based continuous window shift

Synthetic PIV recording pairs of parallel displacements for particle image diameter of $2 \sim 5$ pixels, brightness of $130 \sim 250$, and image number density of 20 without background noise are evaluated with a 32×32 -pixel interrogation window using the traditional FFT-based correlation algorithm, CDWS, and FCTR, respectively. Root-mean-square (RMS) evaluation errors obtained with more than 15,000 displacement vectors in each evaluation case are given in Fig. 1. As shown in Fig. 1, when using the traditional FFT-based correlation algorithm, the evaluation error equals 0 at zero displacement; when the particle image displacement increases to about 0.6 pixels, the evaluation error increases linearly and rapidly up to 0.15. A further increase in the particle image displacement to 1 pixel increases the evaluation error slightly to 0.16. The evaluation error of CDWS has a triangular distribution in the 1-pixel period with its maximum at the midpixel position. The evaluation error of FCTR has a relatively flat distribution in the 1-pixel period, and it is larger than that of CDWS at integer pixels but smaller at the midpixel position.

The CDWS algorithm is related to the traditional FFT-based correlation algorithm but is much better because the large evaluation errors in the particle image displacement region of larger than 0.5 pixels are avoided by using the discrete window shift. If the particle image displacement to be evaluated is restricted within a very small region near 0, e.g. < 0.2 pixels in Fig. 1, much greater evaluation accu-

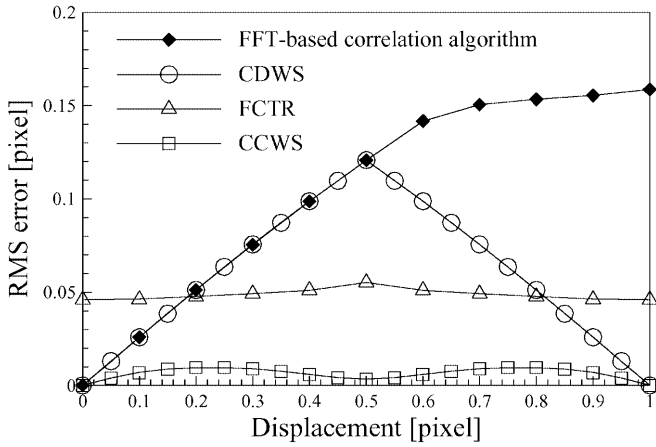


Fig. 1. Dependence of evaluation error on particle image displacement for different algorithms

racy than that of both CDWS and FCTR may be achieved. A simple and effective technique to realize a very small particle image displacement is to continuously shift the interrogation window on the second PIV image in the recording pair. When using the continuous window shift, the gray-value distribution $g_2(i, j)$ cannot be directly “read” from the second PIV image of the recording pair – an interpolation is necessary. We assume that continuous window shifts $X = I + x$ and $Y = J + y$ are needed to determine the gray-value distribution of the second evaluation sample $g_2(i, j)$ from the gray-value distribution of the second PIV image $G_2(i, j)$. Here (I, J) and (x, y) are the discrete and nonnegative subpixel portions of the window shift, respectively. The following bilinear function can be used for the interpolation:

$$\begin{aligned}
 g_2(i, j) = & (1 - x) \cdot (1 - y) \cdot G_2(i + I, j + J) \\
 & + x \cdot (1 - y) \cdot G_2(i + I + 1, j + J) \\
 & + y \cdot (1 - x) \cdot G_2(i + I, j + J + 1) \\
 & + x \cdot y \cdot G_2(i + I + 1, j + J + 1) .
 \end{aligned} \quad (3)$$

The above synthetic PIV recording pairs are also evaluated by using the correlation-based interrogation algorithm with the continuous window shift (CCWS) according to the known displacements, i.e. the actual (real) velocity field. The RMS error of CCWS shown in Fig. 1 is much smaller than that of either CDWS or FCTR.

Since the particle image displacement is unknown, several iterations of the CCWS algorithm to real PIV recordings are necessary to get the final evaluation result. In order to test the iteration performance of the CCWS algorithm, a synthetic PIV recording pair of the rotation movement is evaluated by using the FCTR algorithm, CDWS and CCWS with known particle image displacements, and CCWS with an iterated solution. In the first iteration cycle of CCWS the displacements are given as 0, and the iteration is carried out ten times. The RMS errors and the convergence factor are computed with the evaluation results and are shown in Fig. 2. Here the convergence factor is defined as the RMS difference between

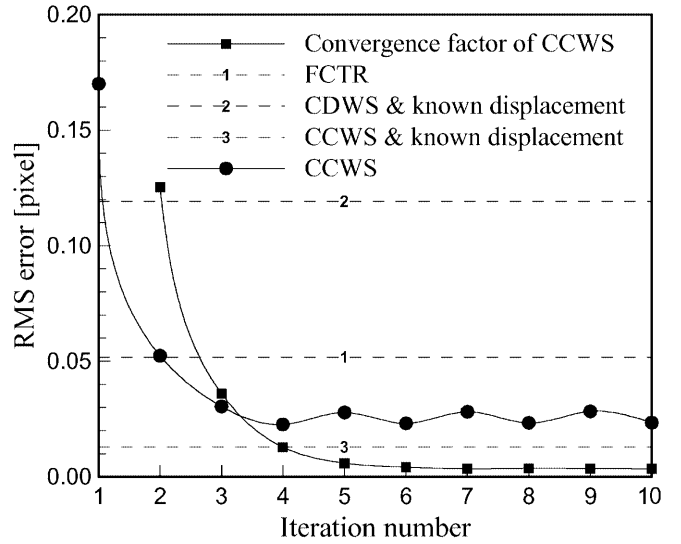


Fig. 2. RMS error and convergence factor at different iteration numbers for CCWS

the evaluation results of the current and previous iteration. Figure 2 shows that the evaluation with CCWS converges after six iterations, but the evaluation error cannot be further reduced when the iteration number is greater than 4. The converged evaluation error of CCWS is slightly greater than that of CCWS with known displacements, but much smaller than those of CDWS and FCTR. Generally, multipass evaluation schemes like CDWS and CCWS have lower computation speeds than single-pass schemes. Because of the interpolation procedure, the computation time for CCWS is about 75% longer than that for CDWS. In comparison to FCTR, CCWS takes 50% more computation time, because it usually needs four iterations but a smaller computation window.

3 Measurement error and peak locking

3.1 Distribution of measurement errors

When N measurements of quantity X_0 are taken, a single measurement sample X_i can be represented as

$$X_i = X_0 + \beta + \varepsilon_i , \quad (4)$$

where β is the bias error, i.e. the constant systematic portion of the measurement error, and ε_i is the random portion of the measurement error that varies around zero. When assuming the sample number N as unbounded, the sum of the random errors is zero. Therefore, the mean of the measurement values is determined as

$$\bar{X} = \frac{1}{N} \sum_{i=1}^N X_i = X_0 + \beta + \frac{1}{N} \sum_{i=1}^N \varepsilon_i = X_0 + \beta . \quad (5)$$

The random error level is usually quantified with the root-mean-square (RMS) fluctuation of the measured values around the mean value, i.e.

$$\sigma = \sqrt{\frac{1}{N} \sum_{i=1}^N (X_i - \bar{X})^2} = \sqrt{\frac{1}{N} \sum_{i=1}^N \varepsilon_i^2} . \quad (6)$$

Instead of ε_i , we refer to σ as the random error in the following text. The RMS difference between the measurement samples and the real value is usually used to quantify the total measurement error:

$$\delta = \sqrt{\frac{1}{N} \sum_{i=1}^N (X_i - X_0)^2} = \sqrt{\beta^2 + \sigma^2} . \quad (7)$$

The bias and random error distributions of CDWS, CCWS, and FCTR are given in Fig. 3 for the synthetic PIV images described in Sect. 2 without background noise. Figure 3a shows symmetrical distributions of random errors with maxima at the midpixel positions and minima at the integer-pixel positions for all the three algorithms. Figure 3b indicates that the bias error distributions in the 1-pixel period are antisymmetric. At integer-pixel positions the bias errors are zero for all the three algorithms. The bias errors of CCWS and FCTR have maximum magnitudes around 1/4- and 3/4-pixel positions and pass through zero at the midpixel point. At the midpixel position the bias error of CDWS does not converge and has a maximum magnitude. The gradient of the bias error for CDWS is negative in the whole period except at the midpixel point. The bias error of FCTR has a negative gradient at integer-pixel positions, and its gradient converges and is positive at the midpixel position. The gradient of the bias error for CCWS is positive at integer-pixel positions, but negative at the midpixel position.

In order to consider the influence of the background noise on the bias and random error distributions, the synthetic PIV recordings used above are overlapped with random noises with intensity of 100. The error distributions of the three evaluation algorithms for the synthetic PIV recordings with random background noise are shown

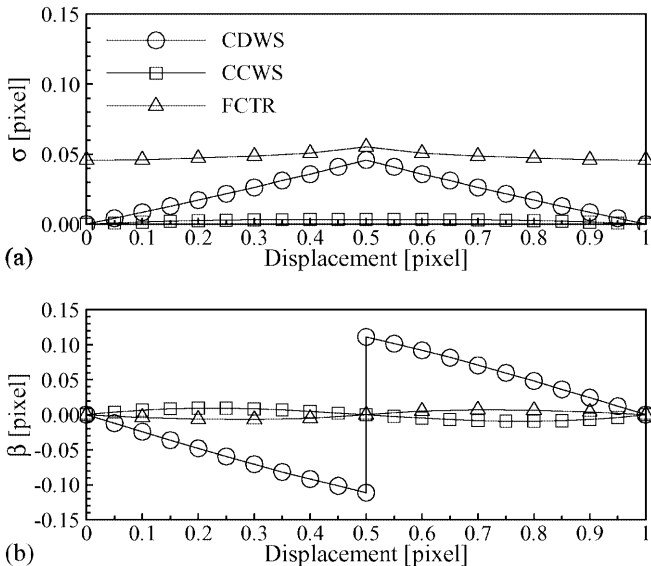


Fig. 3. Random errors (a) and bias errors (b) of different algorithms for PIV images without background noise

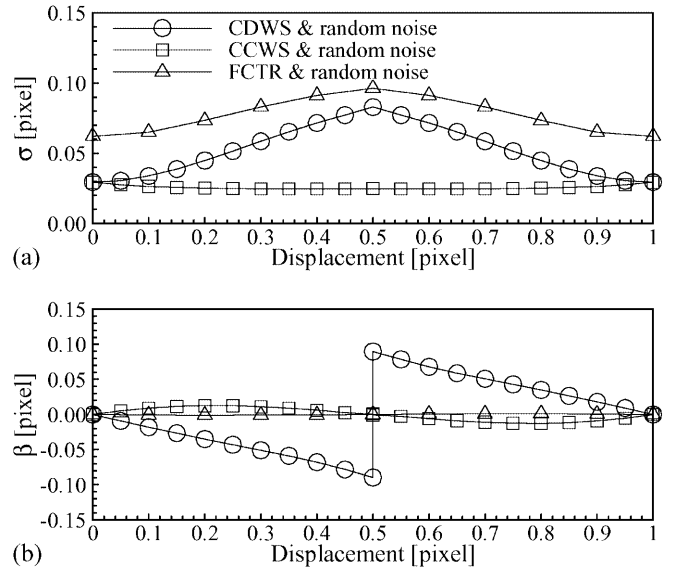


Fig. 4. Random errors (a) and bias errors (b) of different algorithms for PIV images with random background noise

in Fig. 4. Obvious increases in the random errors are observed for all the three algorithms from Fig. 3a to Fig. 4a. For CDWS and FCTR the positions of the maximum and minimum random errors do not change, but for CCWS the positions of the maximum and minimum random errors are switched. Figure 3b and Fig. 4b indicate that the background noise does not change the tendencies of the bias error distributions, but reductions of the bias errors of CDWS and FCTR are observed when the random background noise is added. In both test cases, the random error of CCWS is much smaller than that of CDWS and FCTR, and the bias error of CCWS is very small. Therefore the total error of CCWS is obviously smaller than that of CDWS and FCTR.

3.2

Distribution density and peak locking

As shown in Fig. 5, the probability density for obtaining value X when measuring X_0 has a Gaussian distribution over the region of $[-\infty, \infty]$, i.e.

$$\begin{aligned} p(X) &= \frac{1}{\sqrt{2\pi}\sigma} \cdot \exp\left[-(X - \bar{X})^2 / 2\sigma^2\right] \\ &= \frac{1}{\sqrt{2\pi}\sigma} \cdot \exp\left[-(X - X_0 - \beta)^2 / 2\sigma^2\right] . \end{aligned} \quad (8)$$

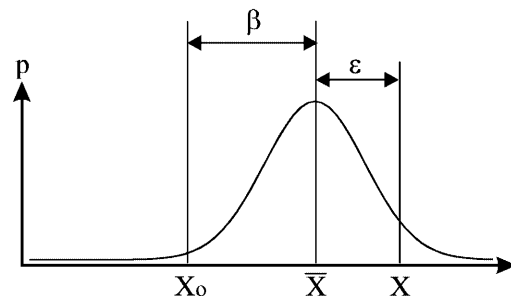


Fig. 5. Probability density of measurement value X

Considering the dependences of bias error β and random error σ on real value X_0 , (8) is rewritten as

$$p(X, X_0) = \frac{1}{\sqrt{2\pi}\sigma(X_0)} \cdot \exp\left\{-\frac{[X - X_0 - \beta(X_0)]^2}{2[\sigma(X_0)]^2}\right\}. \quad (9)$$

Here we define a distribution density for the real value X_0 , i.e. ω , in the variation region $[a, b]$, so that its mean value equals 1, i.e.

$$\frac{1}{b-a} \int_a^b \omega(X_0) dX_0 = 1. \quad (10)$$

The distribution density for the measurement value Ω is determined by

$$\Omega(X) = \int_a^b \omega(X_0) p(X, X_0) dX_0. \quad (11)$$

In PIV experiments the histogram of the particle image displacements $H(X)$ is usually used to reflect the distribution density with following relation:

$$H(X) = M \int_{X-\Delta}^{X+\Delta} \frac{\Omega(X)}{\Delta} dX, \quad (12)$$

where M is the average number of particle displacements in subregion Δ . When Δ approaches zero, the histogram, which is normalized by M , is identical to the distribution density.

To simplify the discussion, we consider here the simplest case, i.e. $\omega = 1$ for $-\infty < X_0 < +\infty$, examples of which are solid body rotation and four-roll mill flow. Thus the distribution density of measurement value X is determined as

$$\Omega_0(X) = \int_{-\infty}^{\infty} \left\{ \frac{1}{\sqrt{2\pi}\sigma(X_0)} \times \exp\left[-\frac{[X - X_0 - \beta(X_0)]^2}{2[\sigma(X_0)]^2}\right] \right\} dX_0. \quad (13)$$

For constant β and σ , Ω_0 is constant and equal to 1. However, because β and σ are periodic functions as discussed in Sect. 3.1, Ω_0 is also a periodic function and varies around the mean value of 1.

Using the error distributions given in Fig. 3 and Fig. 4 and considering the periodicity, the distribution density functions (DDF) are determined for the measured particle image displacement with (13). The DDF are given in Fig. 6. In order to simulate a uniform distribution density $\omega(X) = 1$ of particle image displacements in the synthetic PIV recording, the solid body rotation is adopted. This rotation produces the following spatial distributions of particle image displacements:

$$u = \theta\left(\frac{L}{2} - y\right), \quad v = \theta\left(x - \frac{L}{2}\right), \quad (14)$$

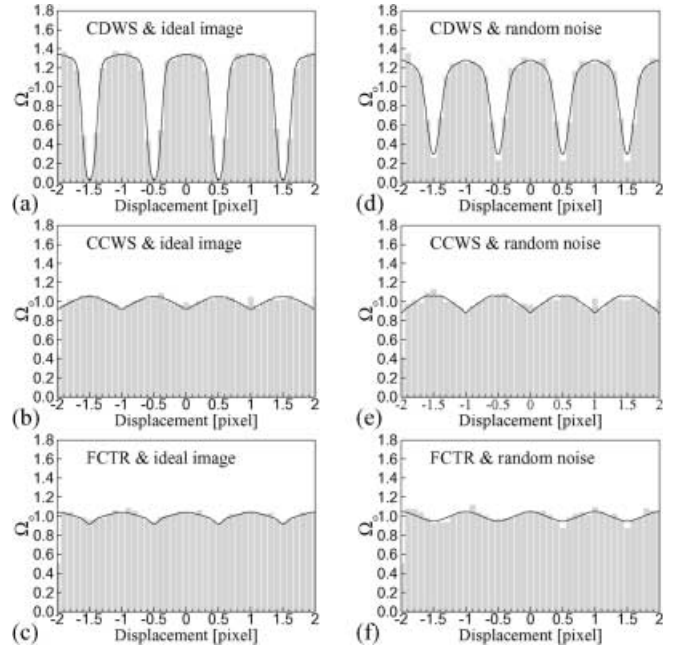


Fig. 6a–f. DDF and histograms of three evaluation algorithms for synthetic PIV images without background noise: **a** CDWS, ideal image; **b** CCWS, ideal image; **c** FCTR, ideal image; **d** CDWS, random noise; **e** CCWS, random noise; **f** FCTR, random noise

where θ is the rotation angle, and L is the side length of the square PIV recording. Apparently, uniform distribution densities are achieved for both particle displacement components in the region of $[-\theta L/2, \theta L/2]$. Here θ is chosen as $\pi/360$, so that the particle image displacement region is $[-4.47, 4.47]$. Except for the displacements, all the parameters for determining the particle images are the same as those used for estimating the DDF in Fig. 6. The rotation PIV recording pairs are evaluated with a high-density grid, and the normalized histograms of the evaluation results, which match the DDF perfectly, are also shown in Fig. 6. Figure 6 indicates that the peaks of the DDF and histograms are “locked” at integer pixels for CDWS and FCTR and at midpixel positions for CCWS. A reduction in the peak-locking effect is clearly indicated for CDWS from Fig. 6a–d, but further quantitative analyses are necessary for CCWS and FCTR.

3.3

Contribution of errors to peak-locking effect

In order to quantify the peak-locking effect in the case of $\omega(X_0) = 1$, a peak-locking factor representing the difference between distribution densities of the real and measurement values is defined as

$$\psi = \int_0^1 |\Omega_0(X) - 1| dX. \quad (15)$$

As shown in Fig. 3 and Fig. 4, the error distributions for CCWS and FCTR are nearly first harmonics for the fundamental frequency of $f = 1 \text{ pixel}^{-1}$, and therefore can be approximately represented as

$$\beta(X_0) = A_\beta \sin(2\pi f X_0) , \quad (16)$$

$$\sigma(X_0) = A_\sigma [1 - \cos(2\pi f X_0)] + \sigma_0 , \quad (17)$$

where A_β and A_σ determine the amplitudes of the bias and random error variations, and σ_0 is the constant portion of the random error. The error distributions for CDWS are sawtooth functions that contain higher harmonics. However, we consider here only the first harmonic to simplify the discussion. Apparently, the sawtooth-shaped error distributions make the peak-locking factor even stronger. As shown in Fig. 7, 21 values of A_β , 13 values of A_σ , and $\sigma_0 = 0.025$ are chosen to investigate the responses of the peak-locking factor.

The peak-locking factors are computed with (13) and (15) for different combinations of the bias and random error distributions and are presented in Fig. 8 in the form of contours. In the bright and dark regions of the figure, the peaks of the DDF are locked at integer-pixel and

midpixel positions, respectively. Figure 8 shows that the peak-locking factor is much more sensitive to the bias error amplitude than to the random error amplitude. Generally, the negative bias amplitude causes peak locking at integer-pixel positions, whereas the positive bias amplitude results in peak locking at midpixel positions. When the bias error amplitude A_β is increased in either the positive or the negative direction, the peak-locking factor increases rapidly. By increasing the random error amplitude A_σ , the peak-locking factor increases and decreases in the integer-pixel- and midpixel-locking cases, respectively. Note that the peaks may also be locked at integer pixels for positive bias error amplitude when the positive random error amplitude is very large. The dependence of the peak-locking factor ψ on A_β and A_σ is shown more clearly in Fig. 9a,b in the form of x - y -plots. When $A_\sigma = 0$, ψ and A_β have a linear relation with a very large negative gradient for $A_\beta < 0$, and with a very large positive gradient for $A_\beta > 0$. When $A_\beta = 0$, the relation between ψ and A_σ is nonlinear with a smaller gradient. The influence of the constant portion of the random error σ_0 on the peak-locking factor ψ is shown in Fig. 9c,d for four combinations of A_σ and A_β . Generally, ψ is not sensitive to σ_0 , but when A_σ and A_β have the same sign, ψ decreases with increasing σ_0 .

3.4

Particle size, number, and interrogation window size

In order to discuss the influence of particle image size on the peak-locking effect, synthetic PIV recording pairs are generated with an average particle number density of 20. In each recording pair the particle images have the same diameter, varying from 1 to 5 pixels. The brightness of the particle images varies randomly between 130 and 250. For each particle image diameter, 11 parallel particle image displacements are simulated to construct the bias and random error distributions in the 1-pixel period. Random background noise of intensity 50 is added. These synthetic PIV recording pairs are evaluated by using FCTR, CDWS, and CCWS algorithms with a 32×32 -pixel interrogation

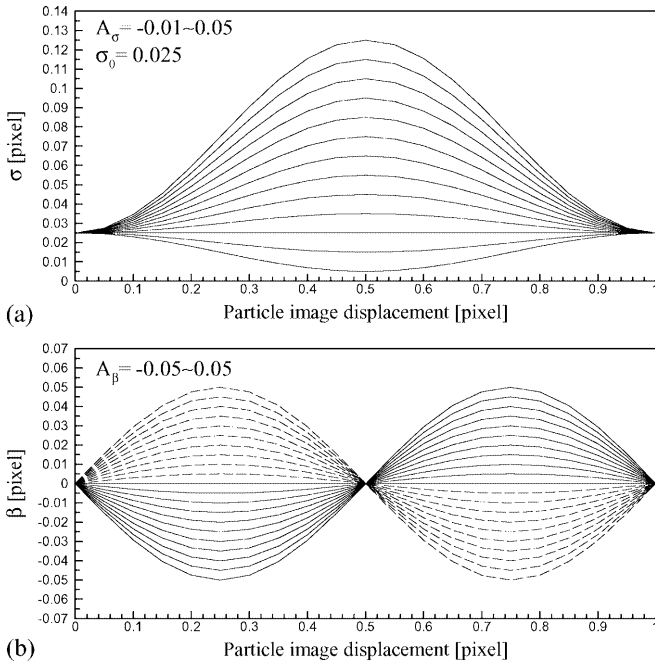


Fig. 7. Simulated random (a) and bias (b) error distributions used to investigate peak-locking effects

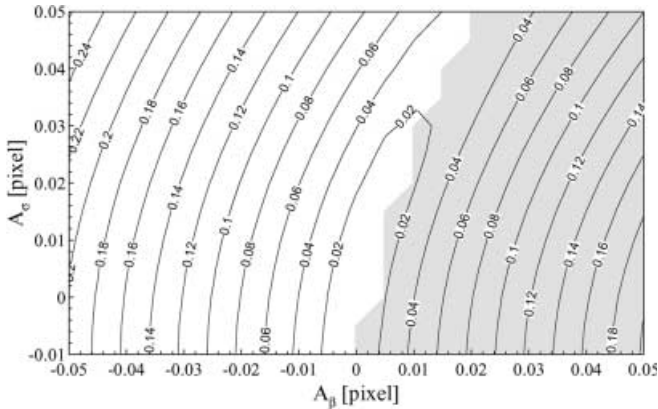


Fig. 8. Contours of peak-locking factor in the A_σ - A_β -plane

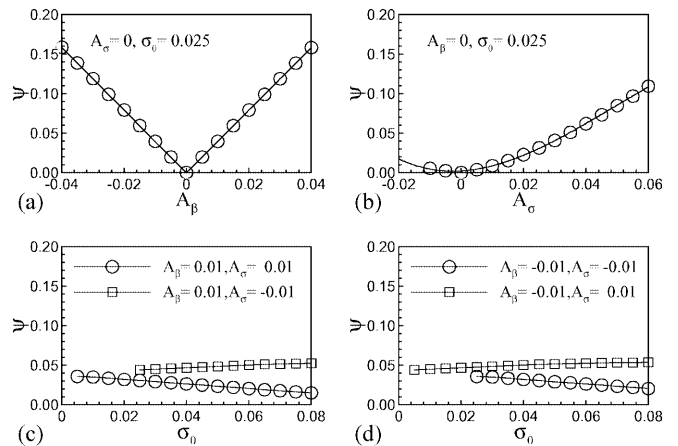


Fig. 9a-d. Dependence of peak-locking factor on A_σ , A_β , and σ_0 : a $A_\sigma = 0$, $\sigma_0 = 0.025$; b $A_\beta = 0$, $\sigma_0 = 0.025$; c $A_\beta = 0.01$, $A_\sigma = 0.01$ (\circ), $A_\beta = 0.01$, $A_\sigma = -0.01$ (\square); d $A_\beta = -0.01$, $A_\sigma = -0.01$ (\circ), $A_\beta = -0.01$, $A_\sigma = 0.01$ (\square)

window. The peak-locking factors and RMS errors of the evaluation results are shown in Fig. 10.

As shown in Fig. 10a, when FCTR is used, the peak-locking factor is large at very small particle diameters, e.g. at 1 pixel, but it decreases rapidly when the diameter increases from 1 pixel to 2 pixels. Further increases in the diameter do not cause obvious changes in the peak-locking factor. For CDWS the peak-locking factor is very large at large particle diameters, decreases to a minimum when the particle image diameter is reduced to about 1.25 pixels, but increases rapidly on further reduction of the image size. When using CCWS the peak-locking factor has a maximum at the particle image diameter of about 1.25 pixels and decreases to a minimum when the particle image diameter increases to 5 pixels or more. Among the three evaluation algorithms, FCTR has the smallest peak-locking factor in most of the diameter range. However, at very small particle image diameters, i.e. 1 pixel, the random error of CCWS has relatively large positive amplitude that reduces the pixel-locking effect at midpixel positions and may even move the peaks to the integer pixels. Therefore, the smallest peak-locking factor among the three evaluation algorithms is observed in Fig. 10a for CCWS in the case of very small particle images. Figure 10b shows the dependences of the RMS evaluation errors on the particle image diameter for the three evaluation algorithms. The RMS error here is an average in the 1-pixel displacement period. The figure indicates that the evaluation errors of FCTR and CDWS are minimal when the particle image diameter is around 1.5 pixels, and they increase when the particle image diameter becomes larger or smaller. The RMS error of CCWS decreases with increasing particle image size; it is nearly as large as those of FCTR and CDWS at very small particle images, but it is much smaller when the particle image diameter is greater than 2 pixels.

To investigate the influence of the particle image number density on the peak-locking effect and the RMS evaluation error, synthetic PIV recording pairs are generated with particle image diameters of 1~3 pixels and brightness of 130~250. The particle image number

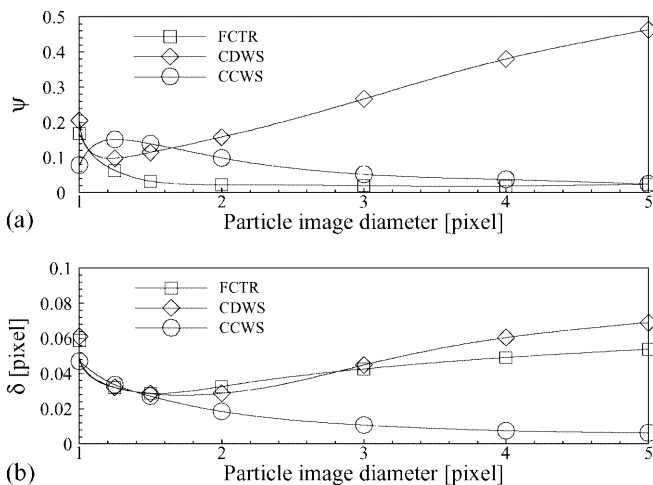


Fig. 10a, b. Influence of particle image size on: a peak-locking factor; b RMS error

density varies from 10 to 40 with a step of 5. The random background noise is added with intensity of 50. The peak-locking factor and RMS evaluation error are computed with the evaluation results of the three algorithms using a 32×32 -pixel interrogation window; the results are given in Fig. 11. Figure 11a indicates that the number of particle images in the interrogation window has nearly no influence on the peak-locking factor. Figure 11b shows that the RMS evaluation error decreases with increasing particle image number density for all the three algorithms, and it is the smallest when using CCWS. The RMS error of FCTR is smaller at high image number densities than that of CDWS, but greater at low image number densities.

To discuss the influence of the interrogation window size, synthetic PIV recording pairs are generated with particle image diameters of 1~3 pixels, brightness of 130~250, particle number density of 40, and background noise intensity of 50. These synthetic PIV recording pairs are evaluated with seven square interrogation windows, whose side length varies from 16 to 64 pixels with steps of 8 pixels. When the side length is not a power of two, a padding technique is used to realize the FFT computation (Gui and Merzkirch 1998). Evaluation results of the three algorithms are used to calculate the peak-locking factor and the averaged RMS evaluation error. The final results are shown in Fig. 12. In Fig. 12a the peak-locking factor for CDWS is very large at the smallest interrogation window (i.e. 16×16 pixels), and it decreases with increased interrogation window size. For FCTR and CCWS the peak-locking factor is much smaller than that for CDWS at small interrogation windows. When the interrogation window size is increased, the peak-locking factor decreases for FCTR, but increases slightly for CCWS. Figure 12b shows that the RMS evaluation error of CCWS is much smaller than that of FCTR and CDWS at small interrogation windows.

3.5 Overexposed and binarized particle images

The previous discussions are based on particle images with a Gaussian gray-value profile. However, in real PIV

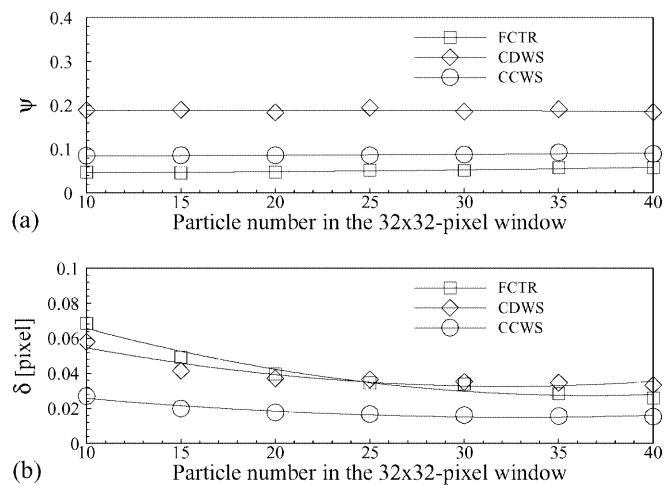


Fig. 11a, b. Influence of particle image number on: a peak-locking factor; b RMS error

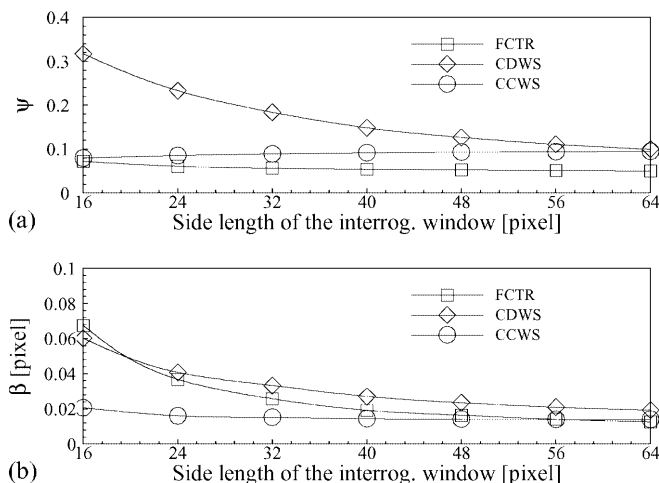


Fig. 12a, b. Influence of interrogation window size on: **a** peak-locking factor; **b** RMS error

recordings the particle images usually do not have a perfect Gaussian gray-value distribution. In many cases, the majority of particles are overexposed in order to clearly image the smaller particles or those particles that are not in the high-intensity portion of the laser light sheet. The overexposed particle image loses part of the structure information in the center, i.e. it does not have a sharp peak, but instead has a flat top. Previous investigations show that the sharp peak of the particle image is essential for obtaining high evaluation accuracy for FCTR and CDWS. Similar to the Gaussian particle images of large diameter, the flat-top particle images may cause large evaluation errors when using FCTR and CDWS. On the contrary, the high accuracy of the CCWS algorithm was preserved for large particle images. Therefore this algorithm may also have good performance for overexposed particle images.

In order to investigate the influence of overexposure on the peak-locking effect and the evaluation accuracy, synthetic PIV recording pairs are generated with Gaussian particle images of diameter $1 \sim 3$ pixels, brightness 250, and image number density 40. Random background noise of intensity 100 is added. To simulate the overexposure, the top of the Gaussian particle images is cut off with a gray-value threshold of 127, and then the gray-value distribution of the particle images is linearly normalized so that the minimum is 5 and the maximum is 250. Considering the worst situation, binary particle images are also obtained from the Gaussian images with the same gray-value threshold. Examples of Gaussian, overexposed, and binary particle images are shown in Fig. 13 in

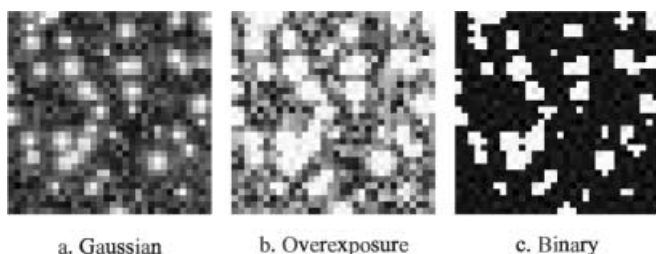


Fig. 13. Gaussian (a), overexposed (b), and binary (c) particle images

32×32 -pixel windows. One important implication or consequence of the thresholding is that the random background noise is removed from the binary recordings because its maximum gray value is below the gray-value threshold.

The synthetic PIV recording pairs of the Gaussian, overexposed, and binary particle images are evaluated with a 32×32 -pixel interrogation window by using the FCTR and CCWS algorithms, respectively, and the dependences of the evaluation errors on the particle image displacement are presented in Fig. 14. The symbol descriptions in Fig. 14d are also applied to all the other subfigures. Figure 14a,d shows that the random error increases when the particle images are overexposed or binarized. The random error is smaller for the binary images than for the overexposed images because the background noise is removed. The amplitude of the random error distribution is larger for the binary images than for the Gaussian and overexposed images, whereas the constant portion of the random error is the largest for the overexposed images because the signal-to-noise ratio is reduced by the overexposure. The bias error distribution in Fig. 14b,e demonstrates inverse tendencies for FCTR and CCWS: when overexposing and binarizing the particle images, the bias error amplitude increases for FCTR but decreases for CCWS. The total measurement error distributions shown in Fig. 14c, f indicate that higher evaluation accuracies can be achieved by using CCWS than FCTR in the three test cases.

According to the random and bias error distributions shown in Fig. 14, DDF of the FCTR and CCWS for the

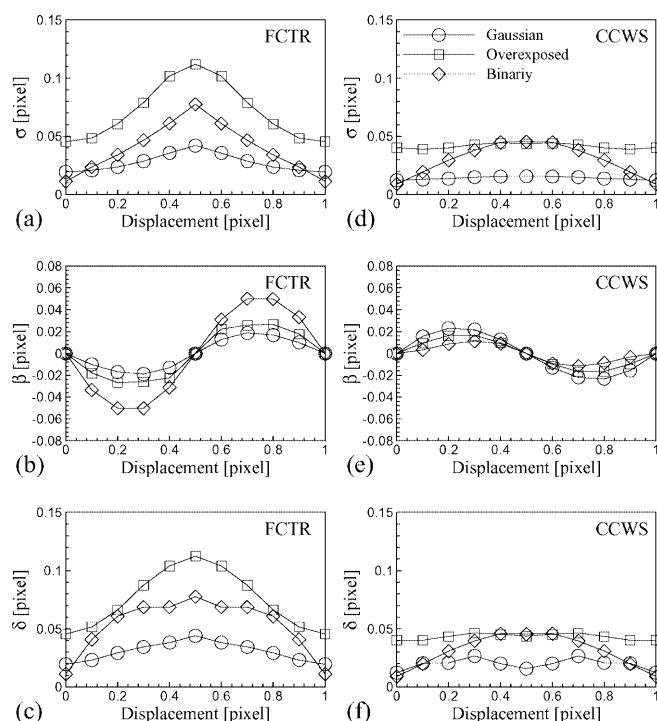


Fig. 14a-f. Evaluation errors of CCWS and FCTR for Gaussian (\circ), overexposed (\square), and binary (\diamond) images: **a** FCTR, random error; **b** FCTR, bias error; **c** FCTR, total measurement error; **d** CCWS, random error; **e** CCWS, bias error; **f** CCWS, total measurement error

Gaussian, overexposed, and binary images are computed and are given in Fig. 15. Normalized histograms are determined by evaluating the synthetic PIV recording pairs with a rotation movement of 0.5° and are shown in Fig. 15 overlapping with the DDF. The DDF and histograms match perfectly in all six cases. A comparison of Figs. 15a and 15d indicates that the peak-locking effects of FCTR and CCWD are nearly the same for the PIV recording pairs with Gaussian particle images. When the particle images are overexposed, see Fig. 15b,e, the peak-locking effect for FCTR becomes much stronger, whereas for CCWS it is reduced slightly. This can be explained by noting that the overexposure increases not only the negative bias error amplitude but also the random error amplitude for FCTR. The peak-locking effect is reduced for CCWS because the overexposure reduces the bias error amplitude. In the case of binary images, because the negative bias amplitude and the random error amplitude are further increased, the peak-locking effect is extremely strong (Fig. 15c) for FCTR. However, since the negative bias amplitude is very small and the random error amplitude is positive, the peak-locking effect is hardly observed for CCWS in the case of binary images (Fig. 15f).

4 Application examples

4.1 PIV measurement in a thermal convection flow

In order to test the evaluation algorithms with real PIV images in the case of overexposure, a pair of singly

exposed PIV recordings taken in a turbulent thermal convection flow (R. Fernandes, personal communication, 2000) is investigated. This PIV recording pair has a size of 1000×1016 pixels. The particle image number density is $20 \sim 30$. The particle image diameter is $2 \sim 5$ pixels. A 32×32 -pixel fraction of the PIV recording is given in Fig. 16, right. The histogram of the digital PIV recording (Fig. 16, left) shows that the particle image is overexposed, i.e. the mean value of the background is about 120 and the maximum probability of the gray value is at 256. This PIV recording pair is evaluated with a 32×32 -pixel interrogation window by using CDWS, FCTR, and CCWS, and the histograms of the evaluation results are given in Fig. 17a–c, respectively. Figure 17a, b present very strong peak-locking effects for CDWS and FCTR. However, the peak-locking effect can hardly be identified when using CCWS, see Fig. 17c.

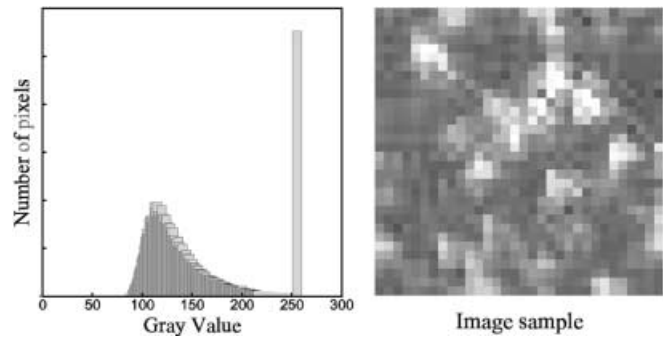


Fig. 16. Histogram (left) and sample (right) of the PIV recording for thermal convection flow

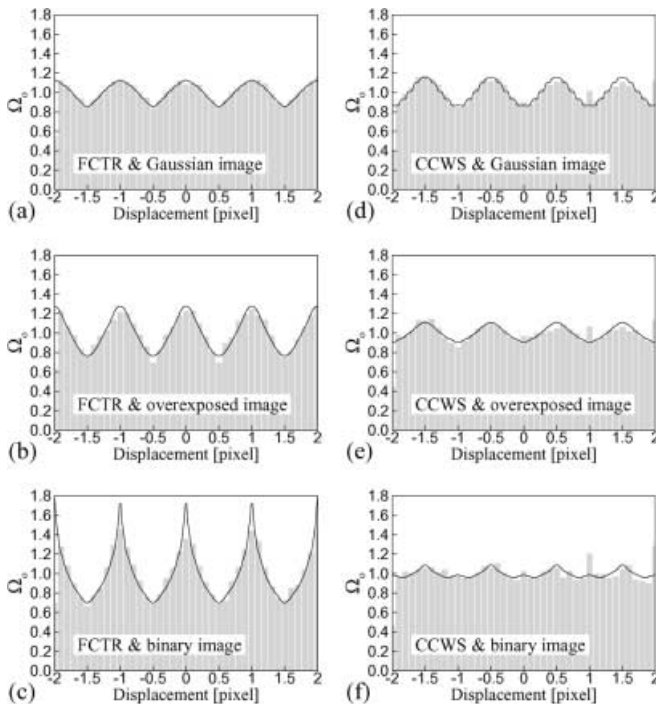


Fig. 15a–f. DDF and histograms of FCTR and CCWS for Gaussian, overexposed, and binary images: a FCTR, Gaussian image; b FCTR, overexposed image; c FCTR, binary image; d CCWS, Gaussian image; e CCWS, overexposed image; f CCWS, binary image

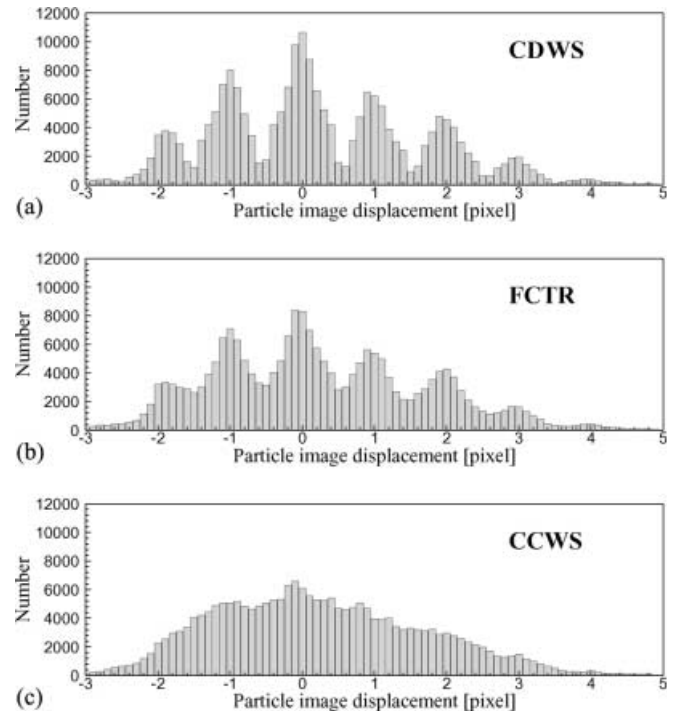


Fig. 17a–c. Histograms of particle image displacements for evaluating the PIV recording pair of the thermal convection flow with different algorithms: a CDWS; b FCTR; c CCWS

4.2

PIV measurement in a wake vortex flow

A pair of PIV recordings is applied to test the evaluation algorithms in the case of very small particle images. This pair is one of several thousand PIV recordings recorded within the EC-funded EUROWAKE project dedicated to the investigation of wake vortices behind a transport aircraft (C. Kaehler, personal communication, 2001; Kompenhans et al. 1999). The measurement was conducted at 1.64 m behind the wing tip, and the field of view of $170 \times 140 \text{ mm}^2$ was imaged with a digital resolution of 1280×1024 pixels. An evaluation sample of 32×32 pixels is shown in Fig. 18, right, and the histogram of the digital PIV recording is given in Fig. 18, left. Figure 18 shows that the PIV recording pair has a reasonable gray-value distribution but very small particle image size. This PIV recording pair is evaluated with a 32×32 -pixel interrogation window using CDWS, FCTR, and CCWS, and the histograms of the evaluation results are given in Fig. 19a–c, respectively. Figure 19a,b demonstrates very strong peak-locking effects for CDWS and FCTR, whereas the peak-locking effect for CCWS is much weaker. This investigation confirms the results given in Fig. 10a at a particle image diameter of 1 pixel. In the case of small particle images, the strong peak-locking effects for CDWS and FCTR result primarily from very large random error amplitudes. However, for CCWS the large random error amplitude reduces the peak-locking effect at midpixel positions, and as shown in Fig. 19c, even causes peak locking at integer pixels.

4.3

PIV measurement in a microchannel flow

A PIV recording pair taken in a microchannel flow (Meinhart et al. 1999) with a digital resolution of 1100×930 pixels is also used to test the evaluation algorithms. A 32×32 -pixel fraction of the PIV recording is shown in Fig. 20, right. The histogram of the PIV recording is given in Fig. 20, left. The particle images do not have perfect Gaussian gray-value distributions because of the low gray-value resolution and high noise ratio. This PIV recording pair is evaluated with a 64×32 -pixel interrogation window in the near-wall region, and the histograms of the evaluation results are given in Fig. 21a–c for CDWS, FCTR, and CCWS, respectively. For CDWS and

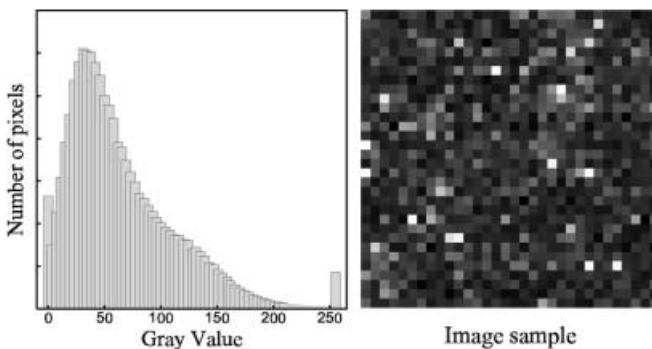


Fig. 18. Histogram (left) and sample (right) of the PIV recording for wake vortex flow

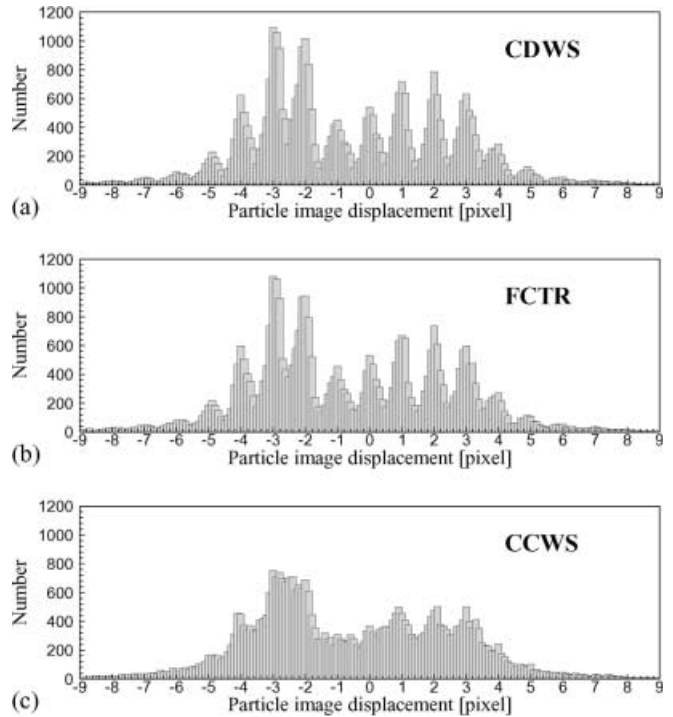


Fig. 19a–c. Histograms of particle image displacements for wake vortex flow: a CDWS; b FCTR; c CCWS

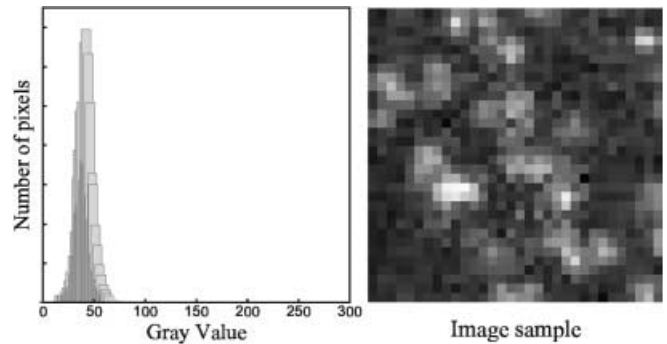


Fig. 20. Histogram (left) and sample (right) of the PIV recording for microchannel flow

FCTR, peak-locking effects can be seen clearly at all the integer pixels. However, the peak-locking effect for CCWS is much weaker and can only be identified at 9.5 and 10.5 pixels.

5

Summary and conclusions

The present work gives a reasonable explanation of the peak-locking phenomenon in the evaluation of digital PIV recordings and provides a method to reduce the peak-locking effect and the measurement uncertainty. On the basis of evaluating error distributions estimated by using synthetic PIV recording pairs, the peak-locking effect is quantitatively investigated with the distribution density functions (DDF) of the evaluated particle image displacements, which match perfectly the histograms obtained by simulations. Detailed analyses indicate that the periodically distributed evaluation bias error is the main reason

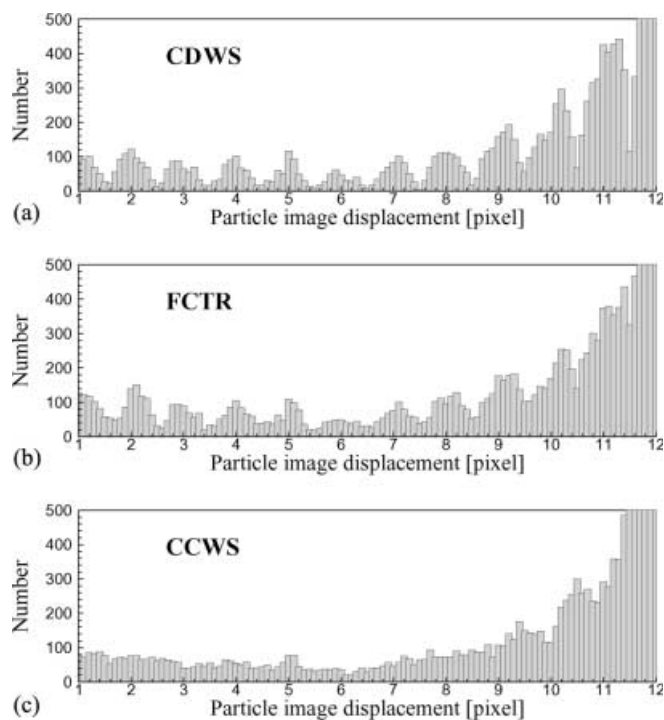


Fig. 21a–c. Histograms of particle image displacements for microchannel flow: a CDWS; b FCTR; c CCWS

for the peak-locking effect. The variation amplitude of the random error in the 1-pixel period is also an important source of peak locking, whereas the constant portion of the random error has little influence on the peak-locking effect. Generally, the peaks of the DDF and the histogram of the particle image displacements are locked at integer pixels when the bias error has a negative gradient at integer pixels and a positive gradient at midpixel positions. In this case the peak-locking effect is further increased by increasing the positive random error amplitude, i.e. the random error is larger at midpixel positions than at integer-pixel positions. In contrast, the peaks are usually locked at midpixel positions when the bias error has a positive gradient at integer pixels and a negative gradient at midpixel positions, and the positive random error amplitude reduces the peak-locking effect and may even move the peaks from the midpixel positions to integer pixels.

The correlation-based interrogation algorithm with discrete window shift (CDWS) has a very strong peak-locking effect at integer pixels for large particle images and small interrogation windows because it has not only very large negative bias error amplitude but also very large random error amplitude in these two cases. The random background noise may reduce the peak-locking effect by reducing the negative bias error amplitude. For very small particles, the peak-locking effect is also very strong because of the very large positive random error amplitude.

The peak-locking effect of the FFT-accelerated correlation-based tracking algorithm (FCTR) is usually not strong for ideal Gaussian PIV images because the negative bias error amplitude is very small, but it becomes significantly stronger when the negative bias error amplitude is

increased by overexposing or binarizing the particle images or by using particle images that are too small. When the particle images are too small, the positive random error amplitude is relatively very large and may dominate the peak-locking effect. For FCTR the peaks of the particle image displacement histogram are locked at integer pixels.

By replacing the discrete window shift (DWS) with the continuous window shift (CWS), the very strong peak-locking effect of the correlation-based interrogation algorithm can be avoided for the cases of large particle images, small interrogation windows, and particle images that are too small. The use of the new evaluation algorithm, i.e. CCWD, also avoids the strong peak-locking effect that may occur when evaluating overexposed or binary PIV recordings and PIV recordings with very small particle images with FCTR. The peaks of the particle image displacement histogram are usually locked at midpixel positions by CCWS, but they may also be locked at integer pixels when the random error variation amplitude is positive and extremely large. Furthermore, the use of CCWS usually achieves lower measurement uncertainty than the use of CDWS and FCTR.

Application examples for turbulent thermal convection flow, vortex flow, and laminar microchannel flow have verified the capability of CCWS to reduce or avoid large peak-locking effects. A recent trend in PIV evaluation algorithms is to consider particle image pattern distortion in the FFT-accelerated evaluation scheme. The continuous window-shifting feature is automatically implemented in these new algorithms. The CCWS enables the high-accuracy capability of the correlation-based interrogation algorithm near zero displacement to be used to great advantage, and shows the promise of the traditional, high-speed algorithm in multi-pass evaluation schemes.

References

- Adrian RJ (1991) Particle-imaging techniques for experimental fluid mechanics. *Annu Rev Fluid Mech* 23:261–304
- Cenedese A, Pagliarunga A (1990) Digital direct analysis of a multiexposed photograph in PIV. *Exp Fluids* 8:273–280
- Fincham AM, Spedding GR (1997) Low cost, high resolution DPIV for measurement of turbulent fluid flow. *Exp Fluids* 23:449–462
- Fei R, Gui L, Merzkirch W (1999) Comparative study of correlation-based PIV evaluation methods. *Mach Graph Vis* 8:571–578
- Gui L, Merzkirch W (1998) Generating arbitrarily sized interrogation windows for correlation-based analysis of particle image velocimetry recordings. *Exp Fluids* 24:66–69
- Gui L, Merzkirch W (2000) A comparative study of the MQD method and several correlation-based PIV evaluation algorithms. *Exp Fluids* 28:36–44
- Gui L, Merzkirch W, Fei R (2000) A digital mask technique for reducing the bias error of the correlation-based PIV interrogation algorithm. *Exp Fluids* 29:30–35
- Gui L, Longo J, Stern F (2001) Biases of PIV measurement of turbulent flow and the masked correlation-based interrogation algorithm. *Exp Fluids* 30:27–35
- Heckmann W, Hilgers S, Merzkirch W, Schlüter T (1994) Automatic evaluation of double-exposed PIV records by an autocorrelation method. In: *Proc IMechE Int Seminar on Optical Methods and Data Processing in Heat and Fluid Flow*, City University, London, paper no C485/021

- Huang HT, Fiedler HE, Wang JJ** (1993) Limitation and improvement of PIV. I. Limitation of conventional techniques due to deformation of particle image patterns. *Exp Fluids* 15:168–174
- Huang HT, Fiedler HE, Wang JJ** (1993) Limitation and improvement of PIV. II. Particle image distortion, a novel technique. *Exp Fluids* 15:263–273
- Keane RD, Adrian RJ** (1990) Optimization of particle image velocimeters. I. Double pulsed systems. *Meas Sci Technol* 1:1202–1215
- Kemmerich T, Rath HJ** (1994) Multi-level convolution filtering technique for digital laser-speckle-velocimetry. *Exp Fluids* 17:315–322
- Kompenhans J, Dieterle L, Vollmers H, Stuff R, Schneider G, Dewhirst T, Raffel M, Kähler C, Monnier JC, Pengel K** (1999) Aircraft wake vortex investigations by means of particle image velocimetry: measurement technique and analysis methods. In: Proc 3rd Int Workshop on PIV, Santa Barbara, USA, 16–18 September
- Lecordier B, Lecordier JC, Trinité M** (1999) Iterative subpixel algorithm for the cross-correlation PIV measurements. In: Proc 3rd Int Workshop on PIV, Santa Barbara, USA, 16–18 September
- Lecordier B, Demare D, Vervish LMJ, Réveillon J, Trinité M** (2001) Estimation of the accuracy of PIV treatment for turbulent flow studies by direct numerical simulation of multi-phase flow. *Meas Sci Technol* 12:1382–1391
- Meinhart CD, Wereley ST, Santiago JG** (1999) PIV measurements of a microchannel flow. *Exp Fluids* 27:414–419
- Okamoto K, Hassan YA, Schmidl WD** (1995) New tracking algorithm for particle image velocimetry. *Exp Fluids* 19:342–347
- Roth GI, Katz J** (2001) Five techniques for increasing the speed and accuracy of PIV interrogation. *Meas Sci Technol* 12: 238–245
- Scarano F, Riethmuller ML** (2000) Advances in iterative multi-grid PIV image processing. *Exp Fluids* 29:51–60
- Sholl MJ, Savas Ö** (1997) A fast Lagrangian PIV method for study of general high gradient flow. In: Proc 35th Aerospace Sciences Meeting and Exhibit, Reno, USA, 6–9 January, AIAA paper 97-0493 (A97-15543)
- Sjödahl M** (1994) Electronic speckle photography: increased accuracy by nonintegral pixel shift. *Appl Opt* 33:6667–6673
- Wereley ST, Meinhart CD** (2001) Second-order accurate particle image velocimetry. *Exp Fluids* 31:258–268
- Wereley ST, Gui L, Meinhart CD** (2001) Flow measurement techniques for the microfrontier. In: Proc 39th Aerospace Sciences Meeting and Exhibit, 8–11 January, Reno, USA, AIAA paper 2001-0243
- Wereley ST, Gui L** (2001) PIV measurement in a four-roll-mill flow with a central difference image correction (CDIC) method, 4th International Symposium on Particle Image Velocimetry, Göttingen, Germany, Sept. 17–19
- Westerweel J, Draad A, Hoeven J, Oord J** (1996) Measurement of fully-developed turbulent pipe flow with digital particle image velocimetry. *Exp Fluids* 20:165–177
- Westerweel J, Dabiri D, Gharib M** (1997) The effect of a discrete window offset on the accuracy of cross-correlation analysis of digital PIV recordings. *Exp Fluids* 23:20–28
- Westerweel J** (2000) Theoretical analysis of the measurement precision in particle image velocimetry. *Exp Fluids* 29:S003–S012
- Willert CE, Gharib M** (1991) Digital particle image velocimetry. *Exp Fluids* 10:181–193
- Willert CE** (1996) The fully digital evaluation of photographic PIV recordings. *Appl Sci Res* 56:79–102